Proceedings of the Canadian Society for Mechanical Engineering International Congress 2021
CSME Congress 2021
June 27-30, 2021, Charlottetown, PE, Canada

Multi-Shaft Reaction Wheel Design for a 2U CubeSat

Nicholas R.H. Popp[1,2], Vignesh Krishnan[1,2], Elijah Vautour[1,2], Maxwell Bauer[1,2], Annalisa Wailand[1,2], Anthony Newton[1,2], Silas Eastwood[2], Suraj Chandrasekaran[1,2], Robert Bauer[1,2,*]

[1]Department of Mechanical Engineering, Dalhousie University, Halifax, Canada
[2]Dalhousie Space Systems Lab, Halifax, Canada
*Robert.Bauer@dal.ca

Abstract — In this paper, a reaction wheel design is presented and proposed for use in Dalhousie University's Low Earth Orbit Reconnaissance Imagery Satellite (LORIS) 2U CubeSat. After estimating a cumulative maximum disturbance torque of 7.16×10^{-7} Nm in low Earth orbit, a flywheel design was developed with a momentum storage of 1.01×10^{-2} Nms. The authors propose to machine the flywheel in a skate-wheel shape to provide a large inertia-to-mass ratio compared to solid-cylindrical designs. A novel three-shaft system is employed wherein a Brushless DC motor shaft is rigidly connected to a spline-toothed inner shaft which transmits power to an outer shaft rigidly fixed to the flywheel. The inner shaft provides torsional flexibility to the system and ultimately reduces the transfer of vibration due to shaft misalignments. Splines and back-to-back angular contact bearings accommodate axial and radial misalignments between the inner and outer shaft experienced during mounting and operation. Finite element analysis was employed to validate the design across worst-case loading scenarios including rocket launch and misaligned inner and outer shafts.

Keywords-CubeSat; reaction wheel; design; disturbance torques; momentum storage; inertia; pointing; ADCS

I. INTRODUCTION

There is a wide range of reaction wheel (RW) designs presented in the existing literature. This paper focuses on a novel reaction wheel design proposed for the Dalhousie University Low Earth Orbit Reconnaissance Imagery Satellite (LORIS) 2U CubeSat. LORIS plans to achieve three-axis attitude control by aligning three of these RWs along mutually-orthogonal axes within the satellite.

In terms of designs, Takehana and Uchiyama [1] propose a spherical RW design to miniaturize conventional reaction wheel systems. Their design rotates a spherical rotor using omni-directional wheels. Krishna *et al.* [2] propose a spoked-flywheel design for a 2U CubeSat to try to obtain high moments of inertia for a given mass of the wheel. They point out, however, that spoked wheels can be challenging to machine and balance. Additionally, Oland and Schlanbusch [3] present a reaction wheel design for CubeSats where the flywheel exhibits a thin inner disc and a thicker outer ring around its periphery to enable a high moment of inertia for a given flywheel mass. The difference in thickness between the inner and outer ring creates what appear to be symmetrical cavities on either side of the flywheel. Kumar *et al.* [4] studied different flywheel shapes for a nanosatellite including a conical disc, modified constant stress disc, and a flat unpierced disc. They selected a solid disc and arranged four RWs in a tetrahedral configuration to retain three-axis control if one RW fails. Manggala *et al.* [5] designed a micro reaction wheel for a 1U CubeSat that consists of a bowl-shaped flywheel that fits the motor in its cavity. Munter *et al.* [6] present a flywheel design for CubeSats that uses a thin inner disc and thicker outer ring, similar in design to Oland and Schlanbusch [3], except that the two cavities on either side of the thin inner disc are not symmetric. Their reaction wheel design uses two deep-groove ball bearings, a stainless-steel flywheel, and a Faulhaber 1509T006 brushless DC motor.

The LORIS RW adopts a design that is similar in geometry and dimensions to Munter *et al.* [6]. While Munter *et al.* [6] use a stainless-steel flywheel, the present authors are considering the use of the MT18C Tungsten alloy due to its high density. Furthermore, instead of using two deep-groove ball bearings, the proposed LORIS RW design uses a pair of angular-contact ball bearings similar to the high-torque reaction wheel design proposed by Nigo *et al.* [7]. The reasoning behind the decision to use a pair of angular-contact ball bearings is because these types of bearings offer high resistance to any misalignments in the shaft [8]. A nut is then used to clamp the inner races of the two bearings together to establish the necessary preload.

Reaction wheels are one of the primary sources of micro-vibration disturbances onboard spacecraft [9] including CubeSats [6]. Sources of these vibrations include unbalanced rotors, misaligned rotors, and defective bearings [10]. Flexibility is, therefore, needed in the system to accommodate any misalignments between the motor shaft and the outer

The authors received financial support from the Canadian Space Agency (CSA) Canadian CubeSat Project and the Natural Sciences and Engineering Research Council of Canada (NSERC).

flywheel shaft. Furthermore, this flexibility helps to avoid excessive forces and vibrations that could cause damage and failure of RW components. Munter *et al.* [6] use an Oldham coupling which connects the motor shaft to the rotor shaft via grooved disks on both shafts. In their design, an intermediate bronze coupling component having perpendicular grooves on opposite sides mates with the grooves on the shaft disks to transmit motor torque. The LORIS RW design couples the motor shaft with the flywheel shaft using a novel multi-shaft design. This design incorporates a thin flexible shaft within the flywheel shaft which connects the motor shaft to the flywheel shaft. The torsional stiffness and terminal coupling of this flexible inner shaft is designed to reduce the potential for excess forces and vibrations due to shaft misalignment.

In this paper, Section II describes the RW momentum storage calculations, Section III presents the final design, Section IV explains the design calculations, while Section V draws conclusions about the design and makes recommendations for future work.

II. Momentum Storage Calculations

The momentum storage requirement of the reaction wheel was determined based on the estimated worst-case environmental disturbance torques for the LORIS CubeSat which is shown in Fig. 1. These disturbance torques include gravity gradient, aerodynamic, solar radiation, and residual magnetic dipole moment torques.

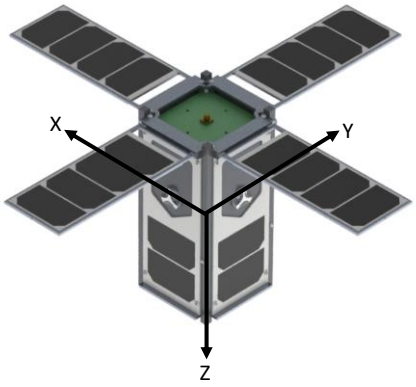

Figure 1. LORIS CubeSat CAD rendering, the nominal body-fixed Z axis points nadir [11]

The maximum aerodynamic torque T_a can be approximated using the following simplified equation [12]

$$T_a = 0.5\rho C_d A V^2 (c_{pa} - c_g) \quad (1)$$

where $\rho = 2.72 \times 10^{-12}$ kg/m^3 is the atmospheric density at altitude, $C_d = 2.25$ is the assumed drag coefficient, $A = 0.022$ m^2 is the assumed exposed surface area, $V = 7665$ m/s is the orbital velocity, and $(c_{pa} - c_g)$ is the difference between the center of aerodynamic pressure and the center of gravity which is assumed to be 0.05 m. The resulting maximum aerodynamic torque is calculated to be $T_a = 1.98 \times 10^{-7}$ Nm.

The maximum magnetic field disturbance torque T_m can be estimated using the following simplified equation [12]

$$T_m = 2DM/R^3 \quad (2)$$

where D is the spacecraft residual magnetic moment dipole which is assumed to be 0.01 Am^2, $M = 7.96 \times 10^{15}$ Tm^3 is Earth's magnetic constant at it poles where it is largest, and $R = 6.784 \times 10^6$ m is the orbital radius at perigee. The resulting value for T_m is 5.10×10^{-7} Nm.

The worst-case gravity gradient and solar radiation disturbance torques were calculated to be 2.08×10^{-10} Nm and 7.97×10^{-9} Nm, respectively. These torques are two to three orders of magnitude smaller than the dominant disturbance torques and thus contribute little to the overall combined disturbance. The summation of the four torque maxima yields a cumulative worst-case disturbance torque of $T_{total} = 7.16 \times 10^{-7}$ Nm. It is assumed that the total worst-case disturbance torque T_{total} is cyclic over one orbit and that the disturbance accumulates in half an orbit. The resulting momentum storage required H can then be approximated as follows [12]

$$H = T_{total}(0.5P)(0.637) \quad (3)$$

where $P = 5562$ s is the orbital period and 0.637 is the average of the absolute value of a sinusoidal function. The resulting momentum storage required is $H = 1.27 \times 10^{-3}$ Nms. Using a design margin of eight gives a momentum storage goal of $H_{des} = 1.01 \times 10^{-2}$ Nms. For a reaction wheel rotor spinning at $\omega_s = 5000$ RPM, this momentum storage goal can be achieved with a rotor moment of inertia about its spin axis I_{RW} of

$$I_{RW} = H_{des}/\omega_s = 1.94 \times 10^{-5} \text{ kgm}^2 \quad (4)$$

This desired rotor moment of inertia was used as the basis for the design of the final reaction wheel assembly (RWA).

III. Final Design

The final RWA is shown in Fig. 2 with its associated design parameters and dimensions given in Table I.

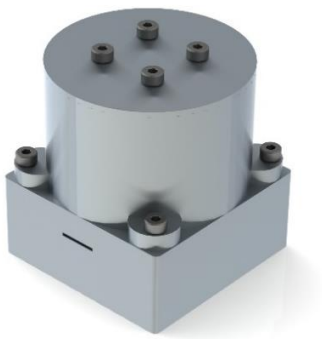

Figure 2. 3D render of final RWA

TABLE I. RWA DESIGN PARAMETERS

Parameter	Value
RWA Mass	221.62 g
Flywheel Mass	133.00 g
Flywheel Moment of Inertia	19.34 kgmm^2
RWA Dimensions	36 × 36 × 36 mm

The individual components of the RWA are shown in Fig. 3. The motor selected for this application is the Maxon 351098 EC 20 Flat brushless DC motor, chosen due to its suitable torque characteristics [13]. The motor is rigidly attached to the base using Scotch-weld 1838 epoxy, which is also used to affix the motor shaft to the inner shaft.

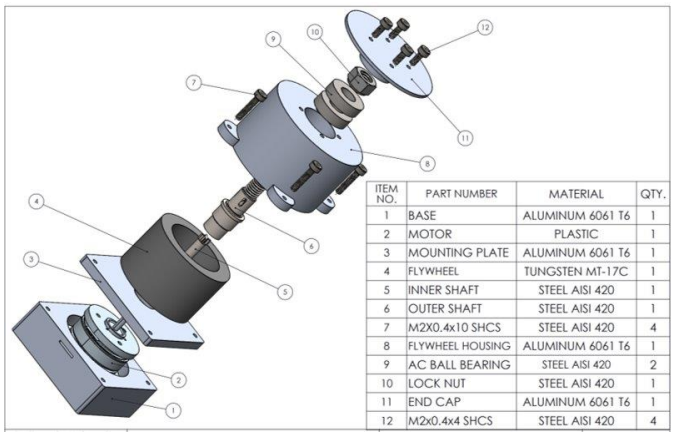

ITEM NO.	PART NUMBER	MATERIAL	QTY.
1	BASE	ALUMINUM 6061 T6	1
2	MOTOR	PLASTIC	1
3	MOUNTING PLATE	ALUMINUM 6061 T6	1
4	FLYWHEEL	TUNGSTEN MT-17C	1
5	INNER SHAFT	STEEL AISI 420	1
6	OUTER SHAFT	STEEL AISI 420	1
7	M2X0.4x10 SHCS	STEEL AISI 420	4
8	FLYWHEEL HOUSING	ALUMINUM 6061 T6	1
9	AC BALL BEARING	STEEL AISI 420	2
10	LOCK NUT	STEEL AISI 420	1
11	END CAP	ALUMINUM 6061 T6	1
12	M2x0.4x4 SHCS	STEEL AISI 420	4

Figure 3. Exploded view of RWA

The inner shaft acts as a flexible coupler between the motor shaft and the outer shaft that drives the flywheel inertia. Torque is transferred between the inner and outer shaft by a spline-toothed coupling system consisting of four splines, as illustrated in Fig. 4.

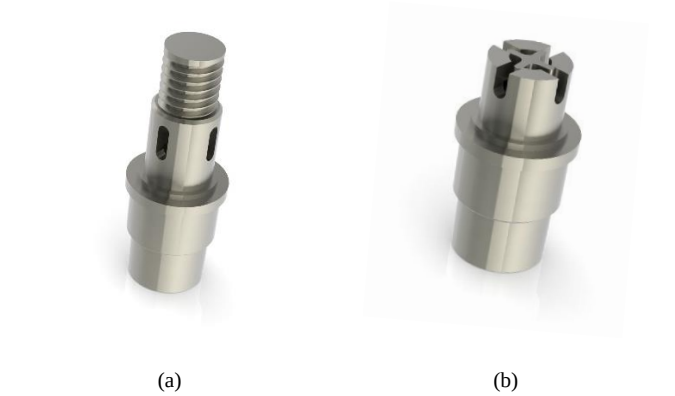

(a) (b)

Figure 4. (a) 3D render of outer shaft (b) 3D render of spline-toothed coupling cross section

The female splines on the outer shaft are created by drilling four slots through the cylindrical outer face of the shaft. The slot sizes are designed to be drilled using a #60-drill bit and are larger than the male splines on the inner shaft to accommodate small radial misalignment between the two shafts.

As shown in Fig. 3, the outer shaft is supported by two angular-contact ball bearings mounted in a back-to-back (DB) configuration. This configuration allows for considerable radial, axial, and moment loading, and significantly increases the rigidity of the flywheel-shaft system [8, 14].

Fig. 5 shows the flywheel designed for the RWA. The flywheel features a skate-wheel design with an off-center hub. The present authors are considering the use of MT18C Tungsten for the flywheel to provide a large mass-to-volume ratio compared to bronze or steel flywheels.

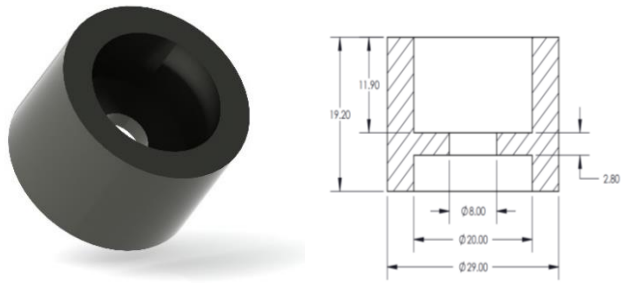

(a) (b)

Figure 5. (a) 3D render of flywheel (b) flywheel cross section (dimensions in mm)

IV. DESIGN CALCULATIONS

A. Launch Load

The largest body loads experienced by the components of the LORIS CubeSat are caused by the accelerations during launch. The corresponding translational and rotational launch accelerations are given in Table II. The main concerns for the RWA caused by these launch loads are the deformation of the inner shaft and the deformation of the fasteners connecting the RWA to the structural members of LORIS.

TABLE II. LAUNCH ACCELERATIONS EXPERIENCED BY LORIS

Direction	Translational Acc. (m/s^2)	Rotational Acc. (rad/s^2)
X	68.67	13.5
Y	39.24	13.5
Z	39.24	13.5

To calculate the deformation of the inner shaft during launch, the inner shaft can be simplified to be a cantilevered beam with the spline heads top face acting as the fixed end. Using simple beam theory and applying the accelerations shown in Table II, the displacement of the inner shaft where it connects to the motor was calculated to be a negligible displacement. This result was validated with a corresponding finite element model of the RWA.

The stress within the fasteners caused by the launch accelerations were approximated by simplifying the mass of the RWA to a point load located at the RWA's center of mass. Using the accelerations shown in Table II, a RWA mass of m_{rwa} = 221 g, and the distances from the center of mass of the RWA to the fasteners, the average stress imparted on the fasteners was calculated to be 998 kPa for each fastener. A finite element model of the RWA determined the stress experienced by each fastener to be 1100 kPa. This result agrees well with the approximated value of 998 kPa and both stress values are well below the yield strength of the fasteners.

B. Bearing Calculations

To ensure the optimal function of the RWA for the duration of the mission, a fatigue life calculation was performed for each angular-contact ball bearing in the duplex pair. The fatigue life is the number of revolutions for which a bearing will operate with 90% reliability [15], and is given as follows [16]

$$L = (C/P)^3 \tag{5}$$

where L is the fatigue life in millions of revolutions, C is the dynamic load rating of the selected bearing, and P is the equivalent radial load applied to the bearing. The fatigue life from (5) was multiplied by a reliability factor of 0.21 as in [16] to yield the number of revolutions for which the bearing will operate with 99% reliability.

Over a proposed mission life of 1.5 years, a bearing spinning at a constant average speed of 3000 RPM undergoes approximately 2.3652×10^9 revolutions. Setting this value as the desired fatigue life with 99% reliability and using C = 695 N [14], the maximum equivalent load P_{max} that can be applied to each bearing is calculated as

$$P_{max} = \frac{C}{(L/0.21)^{1/3}} = 31.00 \text{ N} \tag{6}$$

The equivalent radial load P applied to the bearing was estimated with the following equation [16]

$$P = XF_r + YF_a \tag{7}$$

where F_r = 3 N and F_a = 6 N approximate the radial and axial loads applied to each bearing during operation, respectively, and X = 0.56 and Y = 2.13 were determined from [16] using the static load rating C_{or} of the selected bearing and the values for F_a and F_r. The resulting value of P is 14.46 N, which is lower than P_{max} by a factor of 2.14.

C. Vibrations and Deformation of Flywheel

Imbalance of the flywheel caused by fabrication defects are inevitable and must be accounted for. The maximum acceptable loads on the bearings were determined as described in Section IV-B and the corresponding flywheel imbalance which would produce this load during RW operation was calculated. This imbalance was then used to calculate the permissible tolerances of the flywheel.

The ideal combined mass of the flywheel and shafts is m_{RW} = 101g. Using this mass and the operational flywheel speed of ω_{op} = 5000 RPM, ISO 1940 [17] was used to calculate the product of the operational speed ω_{op} and the permissible eccentricity e_{per} as 0.4 mm/s. The permissible imbalance U_{per} was then calculated using

$$U_{per} = (m_{RW}\, \omega_{op}\, e_{per})/\omega_{op} \tag{8}$$

As described in ISO 1940 [17], the permissible mass imbalance m_{per} can be extrapolated from U_{per} as described by

$$U_{per} = m_{per}\, r_{RW} \tag{9}$$

where r_{rw} is the outer radius of the reaction wheel.

This m_{per} value was added to the ideal mass of the flywheel m_{RW} to develop the volumetric geometry of a flywheel whose dimensions include the maximum permissible tolerances. Finding the difference between this geometry and the ideal geometry of the flywheel yields a difference in volumes. This difference can be simplified to a difference in cross sections where the ideal flywheel cross section is concentric circles, and the non-ideal cross section is a circle within a concentric ellipse. The difference between the major axis of this ellipse and the outer radius of the ideal cross section is the permissible tolerance for the flywheel's radius. This value was calculated to be ±0.058 mm, and a value of ±0.05 mm was used to conform with fabrication standards.

D. Inner Shaft Flexibility and Coupling

The primary purpose of the inner shaft is to provide torsional flexibility to the RWA system. The inner shaft cannot interfere with the outer shaft other than their coupling at the splines. The target torsional stiffness was aligned with those of existing commercial flexible couplings which ranged in torsional stiffness between 30 to 140 Nm/rad [18]. The available length and diameter of the inner shaft are 18 mm and 5 mm, respectively. The torsional stiffness for a cylindrical shaft is related to the shaft length, diameter, and material as follows

$$\frac{T}{\theta} = \frac{J * G}{L} \tag{10}$$

where T/θ is the torsional stiffness, L is the shaft length, J is the shaft torsional moment of inertia for a circular shaft, and G is the shear modulus.

Accounting for thermal expansion and desired axial movement of the inner shaft yields a shaft length of 16.23 mm. Thus, the shaft diameter is the only undefined variable which has a significant effect on the inner shaft's torsional stiffness. Using (10) and setting T/θ to be between 30 to 140 Nm/rad

yielded a range of acceptable diameters from 2.8 to 4.11 mm. A diameter of 4 mm was selected which yielded a torsional stiffness of 125.5 Nm/rad.

Additionally, the secondary benefit of the inner shaft coupling design is its allowance for axial misalignments in the system. By using a spline-toothed coupling, the inner- and outer-shaft axes can allow for a misalignment of up to 0.20 mm in each orthogonal-radial direction – equal to a maximum offset of 0.28 mm between the inner- and outer-shaft rotational axes. This maximum misalignment can be seen in Fig. 6, where the aligned shaft geometry during operation is compared to that of the maximum misaligned shaft geometry.

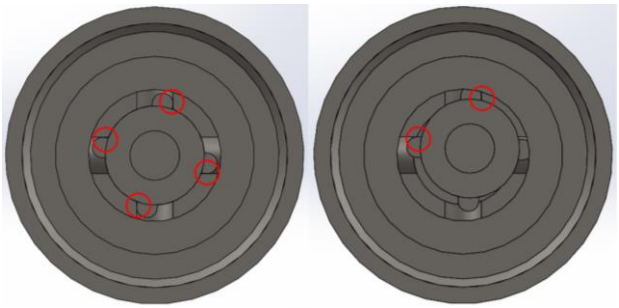

Figure 6. Aligned and misaligned shaft geometry (0.20 mm × 0.20 mm)

As can be seen from Fig. 6, when the shafts are misaligned, the male and female splines contact at only two points rather than four which results in asymmetrical loading conditions. Considering both aligned and misaligned geometry, the worst-case operating conditions were examined to ensure stress failure will not occur. Vibrational loads present during launch represent one of these worst-case scenarios and was covered Section IV-A. In this section, the loads imposed on the inner shaft during an instantaneous change of rotational direction during operation are evaluated.

If the motor is operating at its maximum angular velocity of 5000 RPM and undergoes an instantaneous stop or change in direction, then the inner shaft will stop with it. The outer shaft will, however, continue to rotate and result in a collision between the male and female spline geometry. Using equations from [15], the maximum equivalent-static torque that could occur from this impact was calculated to be 0.66 Nm. This result is equivalent to a 555 N distributed-static load being applied to the end of the inner shaft spline teeth. It should be pointed out, however, that the stall torque of the motor, which is the maximum torque that can be sustained during regular operation, is more than two orders of magnitude lower at 5.29 mNm [13]. Barring catastrophic failure of the motor, the stall torque (and its equivalent-static-load of 3.53 N) represents the worst-case loading conditions for the RWA inner-shaft during regular operation. A finite element analysis (FEA) simulation was carried out to determine the maximum stress which will occur during this loading condition for both the aligned shaft geometry and misaligned shaft geometry described previously. The results of this FEA simulation can be seen in Fig. 7.

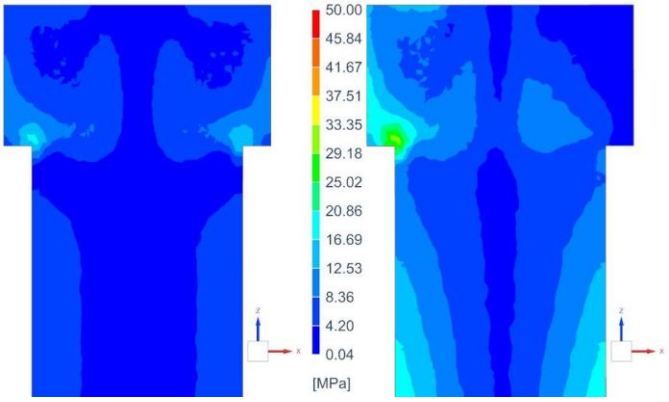

Figure 7. Aligned (left) and misaligned (right) inner shaft cross section stress contours

As can be seen from the left image in Fig. 7, the aligned shaft geometry results in a maximum 3D Von Mises stress of 16.32 MPa experienced in the spline teeth. Alternatively, as can be seen from the right image in Fig. 7, the misaligned shaft geometry results in a maximum 3D Von Mises stress of 30.65 MPa experienced in the spline teeth. Additionally, the asymmetrical loading that occurs during misalignment results in a bending stress being applied to the free length of the inner shaft. Nevertheless, these results show that the stress imposed on the inner shaft during this loading condition is sufficiently lower than the yield strength of the material and should, therefore, not result in either dynamic or fatigue failure.

E. Operation Calculations

Effects caused by the operation of the RWA throughout the LORIS mission was also considered. To identify any RW speeds which may excite resonant frequencies in the RWA structure during operation, a Campbell diagram was created as shown in Fig. 8. This Campbell diagram was produced using rotor dynamics numerical analysis software which implemented the following equilibrium equation for the rotating system [19]

$$[M]\{\ddot{u}\} + ([C] + [G])\{\dot{u}\} + ([K] + [K_c])\{u\} = \{F\} \qquad (11)$$

where [M], [C] and [K] are the system mass, damping and stiffness matrices, respectively, while [G] and [K_c] represent the gyroscopic damping and softening centrifugal stiffness matrices, respectively. The numerical model only included the flywheel, inner shaft, and outer shaft since these are the significant rotating components of the RWA. Rigid body modes and non-rigid body modes that do not intersect with the RW operating speed have been omitted from Fig. 8.

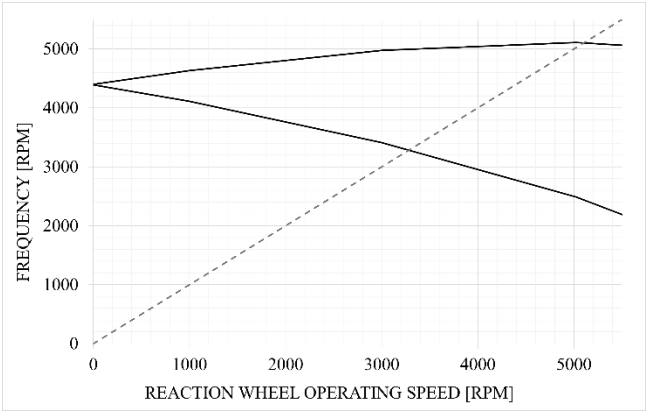

Figure 8. Campbell diagram displaying the significant modes (solid lines) with the flywheel speed (dashed line)

The rotor dynamics analysis produced two modes which are anticipated to be excited directly by the operation of the RW: one mode at 3250 rpm and the other mode at 5075 rpm. Thus, operating speeds near these values are planned to be avoided or quickly passed through during RW operation until physical vibration testing yields the damping values of the RW system near these speeds and the resonant frequency ranges can be confirmed.

V. CONCLUSIONS AND FUTURE WORK

In conclusion, this paper proposes a reaction wheel design for a 2U CubeSat that includes a novel multi-shaft feature with a flexible inner shaft to account for radial misalignment and vibrations in the system. The flywheel inertia was selected to meet the momentum storage required to overcome the anticipated worst-case environmental disturbance torques. The design was validated by considering launch loads, bearing fatigue, vibrations and deformation of the flywheel, inner shaft flexibility and coupling, and operation calculations. Moving forward this design will be machined, assembled, and tested. This RWA design is still in the concept phase and any associated calculations and proposed materials should be verified before this design is launched and deployed into space.

ACKNOWLEDGMENT

The authors would like to thank the members of the Dalhousie Space Systems Lab as well as Neil Laamanen SEATAC Project Coordinator at the Nova Scotia Community College for all of their help and support.

REFERENCES

[1] R. Takehana, K. Uchiyama, “Attitude controller design for a small satellite using spherical reaction wheel system”, 11th Asian Control Conference (ASCC), Gold Coast Convention Center, Australia, Dec 17-20, 2018, pp. 1841-1846.

[2] N. Krishna, et al., “Design and implementation of a reaction wheel system for CubeSats”, IEEE Aerospace Conference, AERO 2018, Big Sky, USA, March 2018, pp. 1-7.

[3] E. Oland, R. Schlanbusch, “Reaction wheel design for CubeSats”, 4th International Conference on Recent Advances in Space Technologies, IEEE, Istanbul, Turkey, June 2009, DOI: 10.1109/RAST.2009.5158296.

[4] S. Kumar, et al., “Design and development of 3-axis reaction wheel for STUDSAT-2”, IEEE Aerospace Conference, IEEE, Big Sky, USA, March 2015, DOI: 10.1109/AERO.2015.7119181.

[5] F. Manggala, et al., “Prototype of micro reaction wheel for Cubesat”, IEEE 13th International Conference on Telecommunication Systems, Services, and Applications, 2019, pp. 209-213.

[6] W. Munter, T. Delabie, D. Vandepitte, “Characterization of reaction wheel micro-vibrations”, Proceedings of ISMA2018 International Conference on Noise and Vibration Engineering and USD 2018 - International Conference on Uncertainty in Structural Dynamics, 2018, pp. 3511 - 3525.

[7] K. Nigo, et al., “Development and qualification test of 1.2-Nm torque reaction wheel assembly with low induced vibration”, IEEE Aerospace Conference, 2018.

[8] R. Budynas, J. Nisbett, “Shigley’s Mechanical Engineering Design”, ninth edition, McGraw Hill, New York, 2011, p. 606.

[9] H. Alkomy, J. Shan, "Modeling and validation of reaction wheel micro-vibrations considering imbalances and bearing disturbances”, Journal of Sound and Vibration, Oct 8, 2020.

[10] M. Le, “Micro-disturbances in reaction wheels”, Technische Universiteit Eindhoven, 2017, p. 32.

[11] Dalhousie Space Systems Lab Chassis Subsystem, CAD Assembly V3.7, 2020.

[12] W. Larson and J. Wertz, (Eds.), “Space mission analysis and design, 2nd Edition", 1992, pp. 353-357.

[13] Maxon Motor Ag, “Maxon EC Flat”, April 2020, PDF file. Retrieved from https://www.maxongroup.com/medias/sys_master/root/8841185132574/EN-277.pdf, pp. 277.

[14] HQW Precision GmbH & The Barden Corporation (UK) Ltd., “High speed spindle bearings”, HQW Precision GmbH & The Barden Corporation (UK) Ltd., PDF file. Retrieved from https://www.hqw.gmbh/res/HQW-BUK-Spindle-Bearing-Catalogue-EN.pdf, 2019, p. 57.

[15] R. Juvinall and K. Marshek, “Fundamentals of machine component design”, 6th ed. Hoboken, New Jersey: John Wiley & Sons, Inc., 2017, p. 273-276, 552.

[16] NSK Ltd., “Miniature ball bearings”, PDF file. Retrieved from https://www.nsk.com/common/data/ctrgPdf/e126h.pdf, CAT.NO. E126h 2011 B-11, NSK Ltd., 2011, pp. 14-16.

[17] International Organization for Standardization, "ISO 1940-1:2003(E)," 15 08 2003. [Online]. Available: https://www.dcma.mil/Portals/31/Documents/NPP/Forms/ISO_1940-1.pdf. [Accessed 01 11 2020].

[18] Huco LLC, "Huco Flexible Couplings," 20 08 2020. [Online]. Available: https://www.altramotion.com/-/media/Files/Literature/Brand/huco-dynatork/catalogs/p-7293-hd-a4.ashx. [Accessed 01 11 2020].

[19] L. Li and R. Grimes, "Introduction of Rotor Dynamics Using Implicit Method in LS-DYNA," in 13th International LS-DYNA Users Conference, Livermore, CA, 2013.